AGU PUBLICATIONS

JGR

Journal of Geophysical Research: Space Physics

RESEARCH ARTICLE
10.1002/2013JA019437

Key Points:
- Examination of Es layer summer maximum phenomenon
- Global distribution of COSMIC-retrieved Es layer
- Es layer formation and wind shear mechanism

Correspondence to:
Y. H. Chu,
yhchu@jupiter.ss.ncu.edu.tw

Citation:
Chu, Y. H., C. Y. Wang, K. H. Wu, K. T. Chen, K. J. Tzeng, C. L. Su, W. Feng, and J. M. C. Plane (2014), Morphology of sporadic *E* layer retrieved from COSMIC GPS radio occultation measurements: Wind shear theory examination, *J. Geophys. Res. Space Physics*, *119*, 2117–2136, doi:10.1002/2013JA019437.

Received 10 SEP 2013
Accepted 22 JAN 2014
Accepted article online 25 FEB 2014
Published online 3 MAR 2014

Morphology of sporadic *E* layer retrieved from COSMIC GPS radio occultation measurements: Wind shear theory examination

Y. H. Chu[1], C. Y. Wang[2], K. H. Wu[1], K. T. Chen[1], K. J. Tzeng[1], C. L. Su[1], W. Feng[3,4], and J. M. C. Plane[3]

[1]Institute of Space Science, National Central University, Chung-Li, Taiwan, [2]Department of Physics, Chinese Culture University, Taipei, Taiwan, [3]School of Chemistry, University of Leeds, Leeds, UK, [4]NCAS, School of Earth and Environment, University of Leeds, Leeds, UK

Abstract On the basis of the Constellation Observing System for Meteorology, Ionosphere, and Climate (COSMIC)-measured fluctuations in the signal-to-noise ratio and excess phase of the GPS signal piercing through ionospheric sporadic *E* (*Es*) layers, the general morphologies of these layers are presented for the period from July 2006 to May 2011. It is found that the latitudinal variation in the *Es* layer occurrence is substantially geomagnetically controlled, most frequent in the summer hemisphere within the geomagnetic latitude region between 10° and 70° and very rare in the geomagnetic equatorial zone. Model simulations show that the summer maximum (winter minimum) in the *Es* layer occurrence is very likely attributed to the convergence of the Fe^+ concentration flux driven by the neutral wind. In addition to seasonal and spatial distributions, the height-time variations in the *Es* layer occurrence in the midlatitude (>30°) region in summer and spring are primarily dominated by the semidiurnal tides, which start to appear at local time around 6 and 18 h in the height range 110–120 km and gradually descend at a rate of about 0.9–1.6 km/h. In the low-latitude (<30°) region, the diurnal tide dominates. The Horizontal Wind Model (HWM07) indicates that the height-time distribution of *Es* layers at middle latitude (30°–60°) is highly coincident with the zonal neutral wind shear. However, *Es* layer occurrences in low-latitude and equatorial regions do not correlate well with the zonal wind shear.

1. Introduction

Ionospheric plasma density irregularities that present as irregular-scattered patches or thin-layered structures, which occur within the normal *E* region (in the approximate height range between 90 and 150 km), are called sporadic *E* (*Es*) plasma irregularities, or *Es* layers, or *Es* clouds, or simply sporadic *E* [*Mathews*, 1998]. In general, compared to the background *E* region plasma density, *Es* plasma irregularities are characterized by relatively intense electron density inhomogeneities that scatter, or refract, or reflect incident EM waves at HF/VHF frequencies [*Whitehead*, 1989]. There are a number of physical processes responsible for the generation of *Es* irregularities, including plasma instability (i.e., gradient-drift instability and two-stream instability) [*Fejer et al.*, 1984; *Farley*, 1985], ion convergence caused by neutral wind shear and/or electric field [*Whitehead*, 1961; *Nygren et al.*, 1984], the neutral turbulence induction effect [*Gurevich et al.*, 1997; *Larsen*, 2000], and particle bombardment effect [*Clemesha*, 1995]. Obviously, *Es* plasma irregularities generated by these different physical processes might be expected to have different properties. For example, the *Es* plasma irregularities excited through two-stream plasma instability, which have a strong bearing on the electroject and are present in a form of plasma turbulences with large vertical extent, occur predominantly in the equatorial and auroral regions [*Kelley*, 1989]. It is generally believed that the *Es* irregularities generated from the wind shear convergence effect, which appear mainly at midlatitudes and are generally absent in geomagnetic equatorial and polar regions, tend to be in a horizontally thin layer with thickness of only a few kilometers [*Whitehead*, 1989]. The *q*-type *Es* irregularities presented in ionogram are characterized by prominent range spreading *Es* traces without a discernible blanketing frequency. The measurements made with ionosondes indicate that this type of *Es* irregularities occurs predominantly in the daytime equatorial region. The physical process responsible for this type of *Es* irregularities in ionogram is thought to be the Bragg scattering of meter-scale field-aligned irregularities generated from gradient-drift instabilities associated with the equatorial electrojet [*Mukunda and Smith*, 1968; *Tsunoda*, 2008]. However, the blanketing *Es* layers that are very likely formed by the wind shear mechanism appear mostly in the midlatitude region during both daytime and nighttime [*Abdu et al.*, 1969; *Tsunoda*, 2008].

The use of ground-based radars operated at various frequencies has been an essential tool for studying *Es* plasma irregularities for more than five decades [*Kelley*, 1989]. It is noteworthy that the plasma irregularities measured by different radar techniques are different. For VHF coherent scatter radars, the radar returns are scattered from field-aligned irregularities with sizes at the Bragg scale (i.e., on a scale of meters) embedded in large-scale *Es* plasma irregularities [*Fejer and Kelley*, 1980; *Chu and Wang*, 1997]. In this context, the radar beam is required to point in the direction perpendicular to the local magnetic field line to effectively detect the radar returns. For incoherent scatter radar, the targets responsible for the backscatter result from very weak fluctuations of the electron density induced by the random thermal motions of discrete electrons [*Farley*, 1966]. For conventional ionosonde operated in the HF band, it is generally believed that the echoes are reflected from patch-like plasma irregularities or thin *Es* layers with a plasma frequency (corresponding to peak electron density in the layers or plasma irregularities) higher than the incident wave frequency [*Whitehead*, 1989]. Nevertheless, the electron density irregularities at sizes from meters to kilometers that may scatter or totally/partially reflect the incident HF waves contribute to the ionosonde echoes in a form of range spread *Es* traces [*From and Whitehead*, 1986; *Maruyama et al*., 2006; *Tsunoda*, 2008; *Chu et al*., 2011]. Therefore, the characteristics of the *Es* plasma irregularities probed by different ground-based radars operated at different frequencies with different sounding techniques may be different.

In addition to ground-based radars, the scintillations of GPS radio occultation (RO) signals detected by low-Earth-orbit satellites, which are caused by the multipath interference of the refracted GPS rays traversing thin *Es* plasma irregularities with sharp vertical electron density gradients, are widely employed to investigate *Es* layer [*Hocke et al*., 2001; *Wu et al*., 2005; *Arras et al*., 2008; *Zeng and Sokolovskiy*, 2010]. *Hajj and Roman* [1998] first proposed the potential of using the intense scintillations of the GPS signal-to-noise ratio (SNR) and bending angle deduced from excess phase to detect the existence of an *Es* layer and its height. *Hocke and Tsuda* [2001] analyzed the correlation between *E* region electron density fluctuation, stratospheric temperature variance, and surface topography in the tropics based on GPS/Meteorology (GPS/MET)-retrieved RO events and suggested a possible link between mountain wave activity and the equatorial *Es* layer occurrence. *Wu et al*. [2005] utilized the scintillations of SNR and phase of GPS RO events recorded by the CHAMP satellites to study the morphology of *Es* layers, including their global coverage, dependence of their activity on geomagnetic dip angle, and their diurnal and seasonal variations. On the basis of GPS RO measurements made with the CHAMP, GRACE A (Gravity Recovery and Climate Experiment), and COSMIC (Constellation Observing System for Meteorology, Ionosphere, and Climate) satellites, *Arras et al*. [2008] investigated the global *Es* layer climatology and showed the effect of the Southern Atlantic Anomaly (SAA) in geomagnetic field intensity on the reduction of the *Es* layer occurrence rate. Using the amplitude fluctuations of the GPS RO signal measured by COSMIC satellites for July 2009, *Zeng and Sokolovskiy* [2010] developed a method to investigate the vertical extent of *Es* layers and showed that the layer thickness ranged from 0.6 to 4 km with a most probable thickness of 1.5 km.

Although the *Es* layers retrieved from GPS amplitude and phase scintillations have been investigated by a number of scientific researchers, the physical process controlling the formation of the RO-measured *Es* layers is not well documented in the literature. *Hocke and Tsuda* [2001] proposed a potential link between mountain wave activity and the occurrence of the GPS/MET RO-observed *Es* layers in equatorial region. However, they did not mention any detailed mechanism for the formation of the RO-observed *Es* layer associated with the wave activity. *Arras et al*. [2009] compared vertical wind shears measured by all-sky meteor radars with the RO-measured *Es* layer occurrence rates from the CHAMP, GRACE, and FORMOSAT-3/COSMIC satellites, and the result shows a good correlation between *Es* layer occurrence and the zonal negative wind shear below 95 km. They therefore suggest that the wind shear theory may be responsible for the formation of the RO-measured *Es* layers in midlatitude region. Nevertheless, to the best of our knowledge, an extensive global examination of the relation between neutral wind shear and the RO-measured *Es* layer occurrence rate above 95 km in different regions for different seasons has not been made. In addition, the horizontal extent of the *Es* layer occurrence region for different seasons has not been analyzed.

Rocket-borne mass spectrometric measurements have demonstrated that *Es* layers are composed of metallic ions such as Fe^+, Mg^+, and Na^+ [*Kopp*, 1997; *Grebowsky and Aikin*, 2002]. These atomic ions, which are produced by meteoric ablation, have very long lifetimes against neutralization in the lower thermosphere because radiative recombination with electrons is extremely slow [*Plane*, 2003]. Although these metallic ions can be converted into molecular ions (e.g., $Fe^+ + O_3 \rightarrow FeO^+ + O_2$), the large concentrations of atomic O

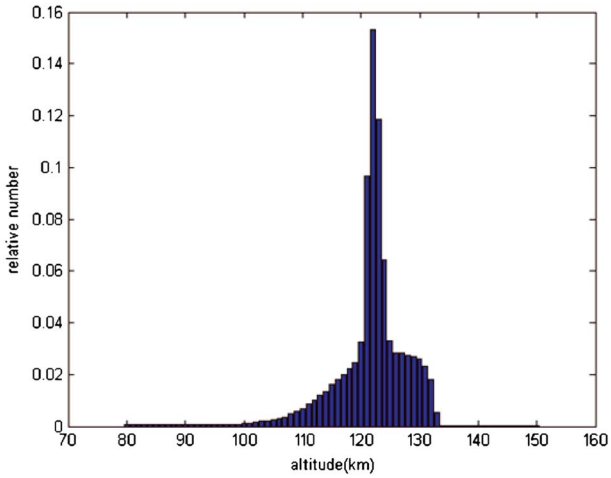

Figure 1. Distribution of ceiling height of COSMIC GPS RO profile at 50 Hz sampling rate for 2008.

above 95 km reduce the molecular ions back to the atomic ions, effectively preventing their neutralization through dissociative recombination with electrons [*Woodcock et al*., 2006].

One of the outstanding issues in ionospheric morphology is the summer maximum (or winter minimum) in the *E*s layer occurrence. *Haldoupis et al*. [2007] proposed that this phenomenon could be explained by a maximum of the meteor influx during the summer solstice season. However, the use of high-power, large-aperture radars to observe meteor echoes shows that the mass influx caused by sporadic meteors, which is significantly larger than that from the meteor showers [*Mathews et al*., 2001], actually peaks in autumn rather than summer [*Janches et al*., 2006]. This result has been confirmed by recent experiment made with Southern Argentina Agile Meteor Radar located at Rio Grande on Tierra del Fuego [*Fritts et al*., 2010]. Therefore, more experimental and theoretical studies are needed to understand the physical process responsible for the phenomenon of the summer maximum in *E*s layer occurrence.

In the present study, the scintillations of the GPS signal amplitude and excess phase measured by the FORMOSAT-3/COSMIC satellites from July 2006 to May 2011 are employed to study the global behavior of *E*s layers, including diurnal and seasonal variations, latitudinal and longitudinal distributions, spatial coverage of *E*s layer occurrence, and geomagnetic influence. A plausible mechanism to explain the summer maximum in *E*s layer occurrence is also investigated. Section 2 describes the criteria for selecting *E*s layers from the amplitude and excess phase of the COSMIC-measured GPS RO profiles. The general behaviors of the *E*s layers are presented in section 3, including vertical and horizontal distributions, and diurnal and seasonal variations. In section 4, on the basis of the wind shear theory combined with a number of models —the HWM07 (Horizontal Wind Model) neutral wind model [*Drob et al*., 2008], the Mass Spectrometer and Incoherent Scatter (MSIS) atmospheric model, and the Whole Atmosphere Community Climate Model (WACCM) [*Feng et al*., 2013]—the global distributions of Fe^+ concentration flux for different seasons are simulated to compare with the COSMIC measurements. The result shows that the wind shear theory can mostly account for the summer maximum in *E*s layer occurrence. In section 5, other properties of the RO-measured *E*s layers, such as geomagnetic control, lightning effect, etc., are examined and discussed. Section 6 contains our conclusions.

2. Data Analysis

Previous studies of RO-measured *E*s layers are based on the GPS signal profiles of the amplitudes and excess phases at 50 Hz sampling rate [*Wu et al*., 2005; *Arras et al*., 2008; *Zeng and Sokolovskiy*, 2010]. Note that the ceiling heights of the 50 Hz GPS RO soundings for the COSMIC profiles are mostly between 120 and 122 km, lower than those for the CHAMP and GRACE profiles (about 140 km) [*Arras et al*., 2010]. Figure 1 shows the ceiling height distribution of the COSMIC 50 Hz GPS RO profiles for 2008. As indicated, more than 50% of the ceiling heights are distributed in the height range between 119 and 125 km with a peak occurrence at 122 km. As a consequence, the detection probability of *E*s layers above 122 km for the COSMIC 50 Hz GPS RO profiles will tend to be systematically low, leading to a potential error in the height distribution of the retrieved *E*s layer occurrence rate and resulting in a biased *E*s layer morphology. However, the upper boundaries of the COSMIC-retrieved RO profiles at a 1 Hz sampling rate (which covers almost the entire ionosphere from about 60 km to 800 km) are usually in the topside ionosphere and well above the *E* region. Therefore, if the *E*s layer can be effectively extracted from the 1 Hz COSMIC RO profiles based on relevant data selection criteria, an unbiased global behavior of the *E*s layers should be acquired.

Several data selection criteria for extracting *Es* layers from RO-measured perturbations of the amplitude SNR and excess phase of the GPS signal have been proposed. For example, *Hocke and Tsuda* [2001] and *Hocke et al*. [2001] calculated fluctuations of the electron density transformed from the GPS RO-observed total electron content (TEC) in the *Es* region, which is proportional to the difference of the GPS L1 (1.575 GHz) and L2 (1.227 GHz) excess phases, to represent *Es* layer activity. *Wu et al*. [2005] extracted the RO-observed GPS SNR and excess phase fluctuations using a high-pass filter and then used the maxima in the SNR and excess phase perturbations to represent an *Es* layer event. *Arras et al*. [2008] identified an *Es* layer event from the GPS RO-measured L1 SNR profile by comparing the calculated standard deviation of the highly perturbed components extracted from the normalized SNR profiles through a high-pass filtering process with a threshold level that was determined empirically. In contrast, *Dou et al*. [2010] performed a least squares quadratic fit to the RO-retrieved COSMIC electron density profile in the height range 70–150 km to obtain the background electron density profile. The peak value of the background-removed electron density profile, when it is at least 2 times larger than the background value, is then identified as the *Es* layer event.

In this study, on the basis of the methods proposed by *Wu et al*. [2005] and *Yang et al*. [2009], we develop a relevant data selection procedure to extract *Es* layer events from the RO-measured COSMIC profiles of the GPS L1 and L2 SNRs and excess phases at a 1 Hz sampling rate. Note that the *F* region plasma irregularities with highly fluctuating electron densities may severely disturb the GPS-measured TEC (or excess phase) and RO-retrieved electron density profiles [*Yang et al*., 2009; *Chu et al*., 2010]. We therefore first use the data quality control criteria developed by *Yang et al*. [2009] to reject the COSMIC profiles influenced by *F* region plasma irregularities from the raw COSMIC data base. About 3–5% of the raw COSMIC profiles are screened out by this quality control procedure. In addition, there are mounting evidences that geomagnetic activity may impact on sporadic *E* layer properties, including *Es* layer occurrence, peak electron density, and blanketing frequency [*Yinn-Nien*, 1965; *Batista and Abdu*, 1977; *Ritchie and Honary*, 2009]. In order to avoid the possible effect of geomagnetic disturbances on the general behavior of the *Es* layers deduced from the COSMIC profiles, data with $Kp \leq 3$ that is considered to be quiet geomagnetic condition are employed in the following analysis. We then apply a high-pass filter with a 3-point equal weight to these sifted COSMIC profiles of the L1 and L2 amplitude SNR and excess phase to extract the respective perturbation components caused by the multipath interference effect of the *Es* layer on the GPS rays. The filtering processes are performed twice for the excess phase and once for the SNR profiles such that the perturbation components can be significantly highlighted from the background noises. It is noteworthy that the excess phase (or propagation phase delay) ΔL of the GPS signal, which results from the phase velocity of the GPS signal propagating in the ionosphere (which is larger than the speed of light) is inversely proportional to the square of the GPS carrier frequency and is given by

$$\Delta \mathrm{L} = \frac{40.323}{f^2}\mathrm{TEC}$$

where f is the GPS carrier frequency (in Hz), TEC is ionospheric total electron density content (el/m^2) along the GPS propagation path, and ΔL is expressed in meter. It is therefore expected that the ratio of the excess phase ΔL_2 of the L2 (1.227 GHz) frequency to the excess phase ΔL_1 of L1 (1.575 GHz) frequency for true *Es* layer events that are physically meaningful will be about 1.65 (that is, approximately equal to the square of the ratio of the L1 frequency to the L2 frequency).

From the above argument, in this study, the criteria of selecting an *Es* layer event from the sifted COSMIC profiles with 1 Hz sampling rate are as follows: (1) the amplitudes of the L1 and L2 phase perturbations are both larger than 5 cm, (2) the excess phase ratio of ΔL_2 to ΔL_1 is within the range 1.5–1.8, and (3) the amplitude of the perturbation of the normalized L1 SNR (i.e., SNR1/SNR0) is greater than 0.01, where SNR0 denotes the background mean value of the GPS L1 SNR. With these criteria, we believe the erroneous *Es* layer induced by instrument and measurement noises that appear in the form of spikes [*Wu et al*., 2005] can also be largely removed. Figure 2 shows the original (top row) and perturbation (bottom row) profiles of the SNRs and excess phases for the L1 and L2 channels, in which the L1 and L2 SNR perturbations are normalized by their respective mean SNR values. The height of the *Es* layer is defined as the altitude where the major peaks of the L1 and L2 excess phases and SNR perturbations simultaneously occur, as shown in the bottom row of Figure 2. Figure 3 compares scatter diagrams of the normalized SNR1 versus L1 phase perturbation and L1 phase perturbation versus L2 phase perturbation before (top row) and after (bottom row) the data pass the *Es*

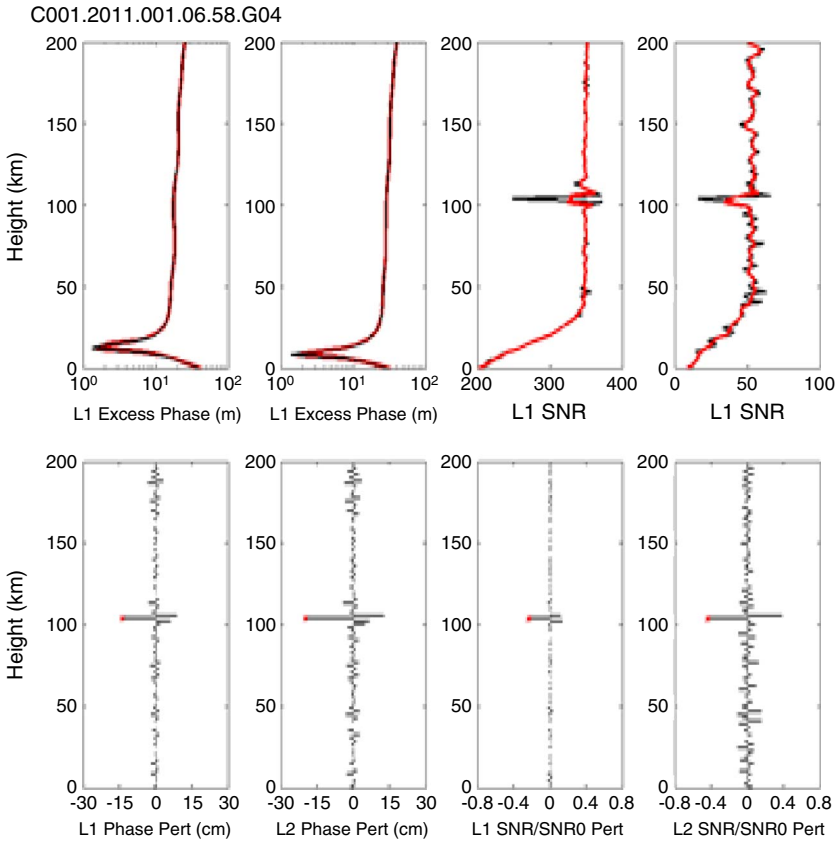

Figure 2. (top row) Raw profiles (black curves) and smoothed profiles (red curves) of the COSMIC-measured excess phase and SNR for L1 and L2 GPS frequencies, in which the smoothed profiles are obtained by applying a low-pass filter with 3-point equal weight to the raw profiles; (bottom row) perturbation components of the excess phase and SNR profiles for L1 and L2 frequencies, which are obtained by removing the smoothed profiles from the raw COSMIC profiles.

layer event selection criteria. Note that the negative slope of the scatter pattern of the L1 versus L2 phase perturbations is caused by the filter-induced out-of-phase effect on the excess phase profiles during the filtering process. It is obvious from Figure 3 that, after sifting the COSMIC data based on the above mentioned data selection criteria, the magnitude of the normalized SNR variation is positively correlated to that of the excess phase perturbation, which is in agreement with the theoretical analysis of the RO-measured GPS phase and SNR perturbations caused by an *Es* layer [*Wu*, 2006]. This feature suggests that the data selection procedures and criteria that we have developed in this study can extract true *Es* layer events from the GPS amplitude and excess phase scintillations of the COSMIC RO measurements at 1 Hz sampling rate in the geomagnetically quiet ($Kp \leq 3$) conditions. On the basis of these selected data, the *Es* layer morphology is now investigated.

3. Observations

Figure 4 shows the global distributions of the total occurrence number of the COSMIC-retrieved *Es* layer binned within a grid of 5° × 5° for the period from July 2006 to May 2011 (left) and the global distribution of the total number of COSMIC 1 Hz radio occultation measurements in *Es* region for the same period and grid resolution (right). Inspecting Figure 4 shows that, because of the orbit configuration of the COSMIC satellites, there is a latitudinal dependence of the number of COSMIC RO measurements, with more frequent occurrences in midlatitudes (especially in the latitudinal zones around ±20° and ±50°) compared with the equatorial and high-latitude regions. This latitudinal dependence should be taken into account in the estimate of the global distribution of *Es* layer occurrence from the COSMIC RO measurements.

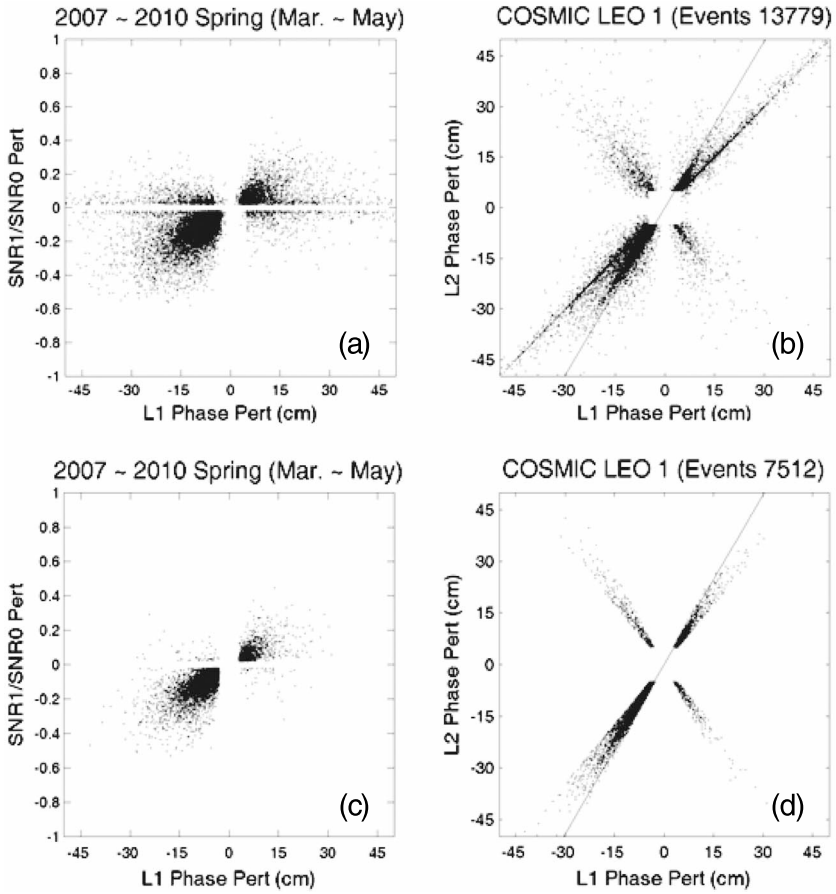

Figure 3. (top row) Scatter diagrams of normalized SNR versus excess phase perturbation for GPS L1 frequency (left) and L1 excess phase perturbation versus L2 excess phase perturbation (right) before applying the data selection criteria to the respective parameters, in which SNR1 and SNR0 are, respectively, the perturbation component and the background mean value of the L1 SNR; (bottom row) Same as Figure 3 (top row) but for the data passing the selection criteria of the *Es* layer event.

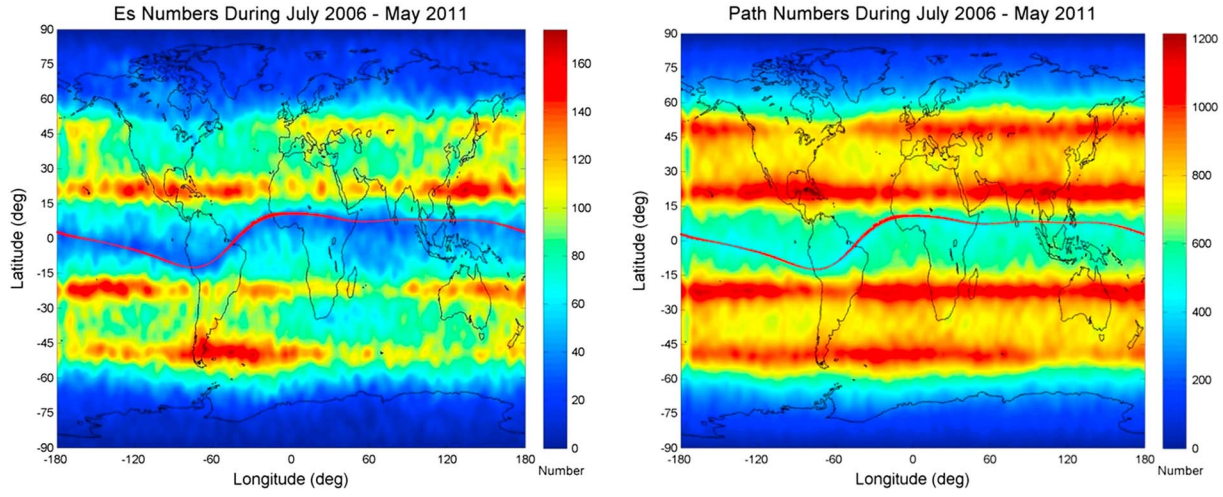

Figure 4. (left) Global distribution of total occurrence number of the COSMIC-retrieved *Es* layer binned within a grid of 5° × 5° for the period from July 2006 to May 2011. (right) Global distribution of total number of COSMIC radio occultation measurement in *Es* region for the same period and grid resolution.

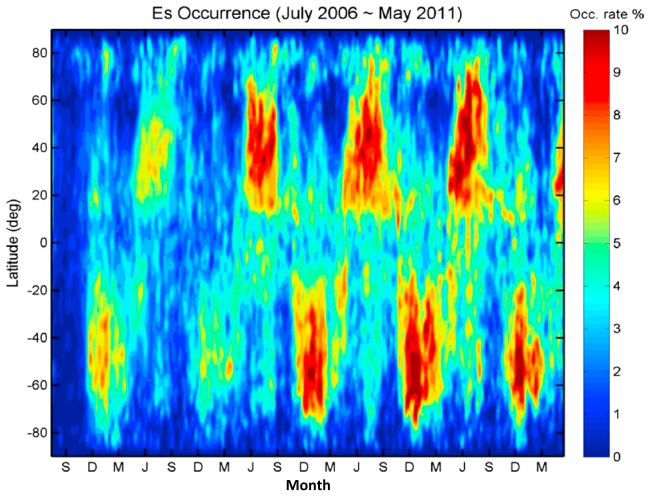

Figure 5. Latitude-month variations in the *Es* layer occurrence rates.

Figure 5 depicts the latitude-month variation in the *Es* layer occurrence rate, in which monthly data from July 2006 to May 2011 are presented. As shown, *Es* layers occur predominantly in the northern (southern) summer hemisphere over a span of about 5 months from May to September (from November to March), with the peak occurrence rates in July (January), i.e., 1 month delay after the summer solstice of June (December). We will show later that this summer maximum (winter minimum) behavior in the *Es* layer occurrence can be satisfactorily explained in accordance with neutral wind shear effect.

Figure 6 presents global distributions of the *Es* layer occurrence rate for different seasons, in which solid curves represent geomagnetic latitude contours. This figure demonstrates that *Es* layer peak occurrence rates within 50°–60° geomagnetic latitude are a factor of 1.5–2 larger in summer compared with the equinoxes. In addition to the Indian Ocean–southern

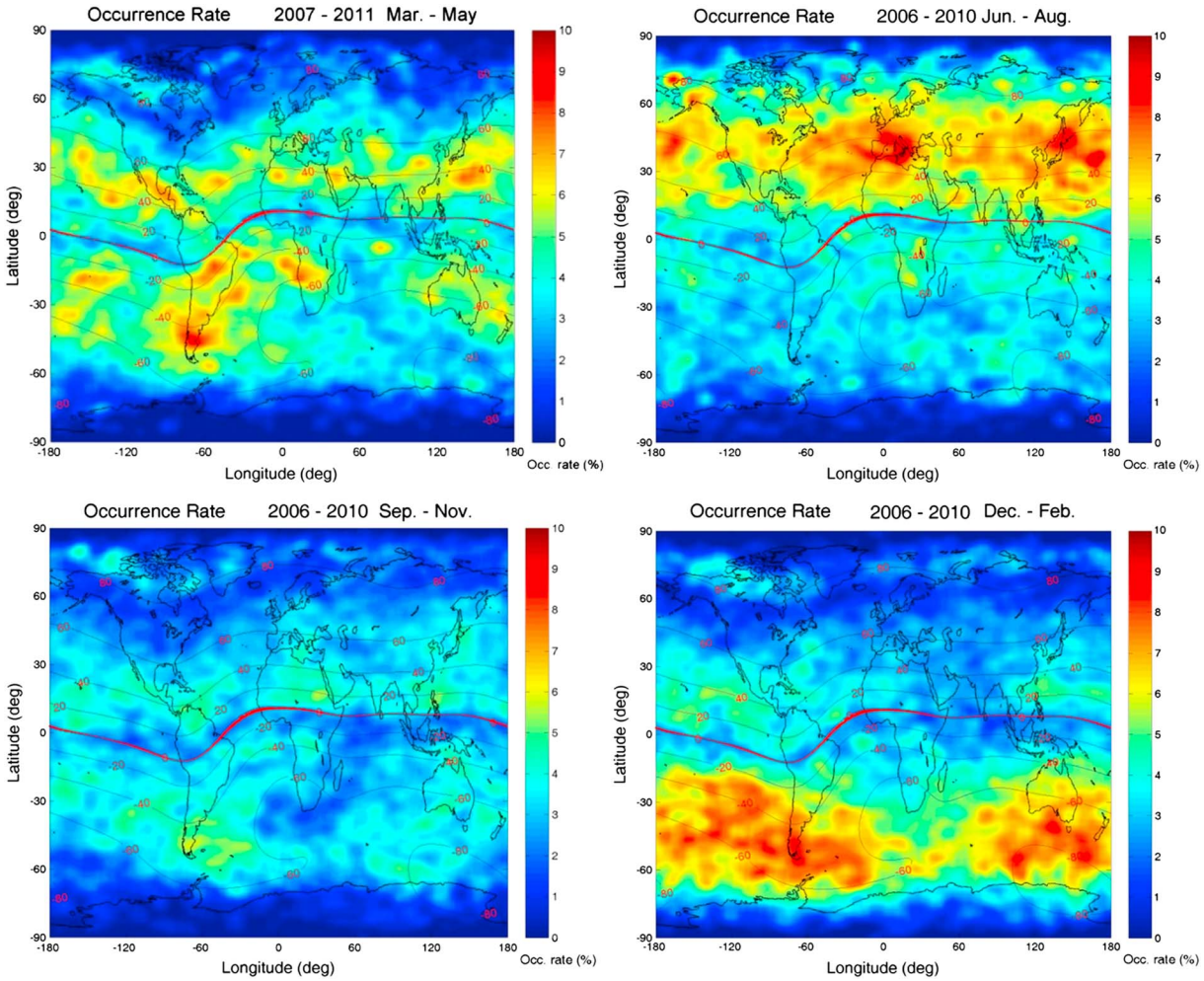

Figure 6. Occurrence rate of COSMIC-retrieved *Es* layer for different seasons. Thin curves signify geomagnetic latitude contours and the thick curve is the geomagnetic equator.

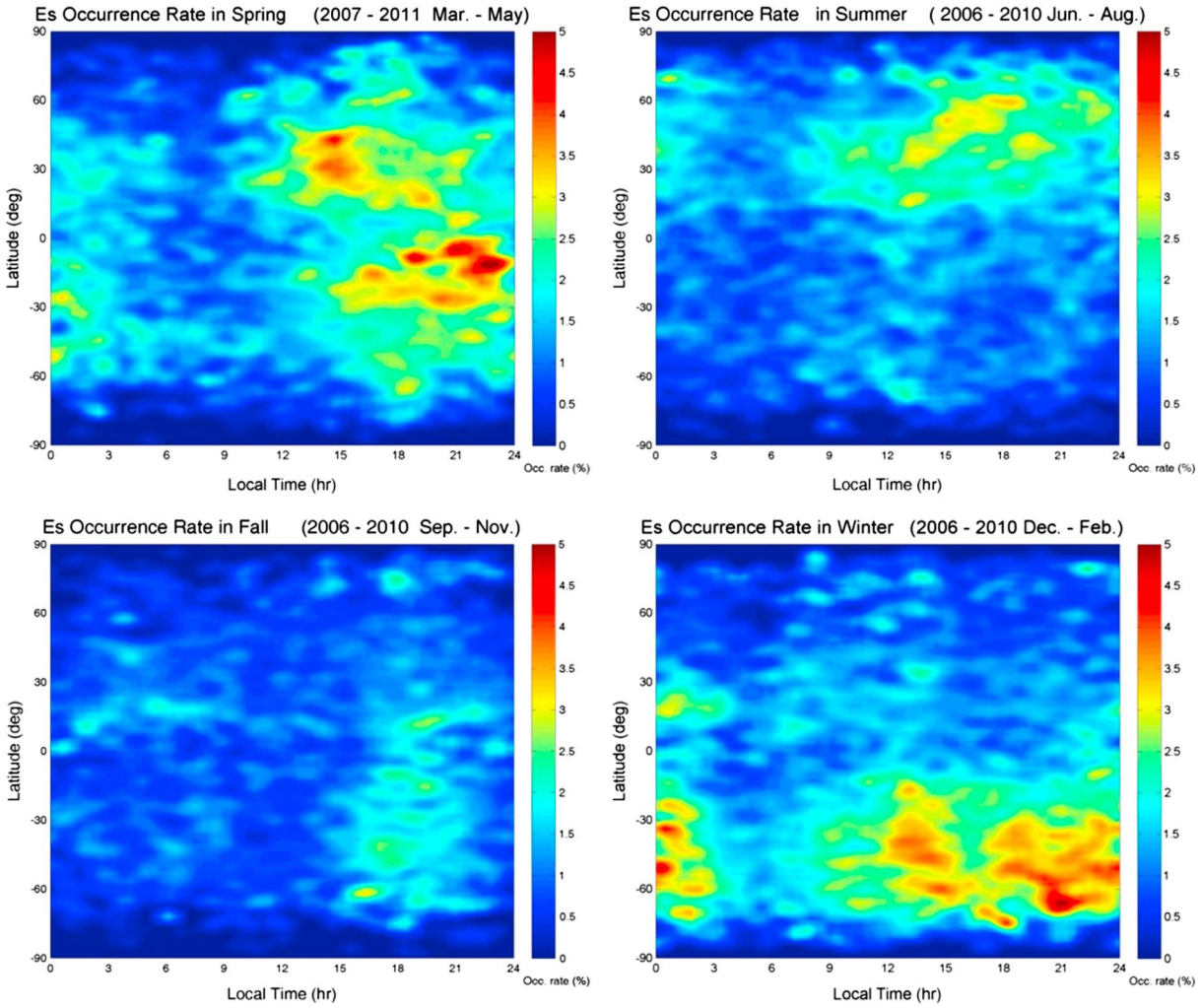

Figure 7. Latitude-local time distribution of the occurrence rate of the COSMIC-retrieved *Es* layer for different seasons.

African region close to the Southern Atlantic Anomaly (SAA) zone, the decrease of the *Es* layer occurrence rate in the northern American region is also seen in Figure 6. These features, combined with the fact that the *Es* layer occurrence basically follows the geomagnetic latitude contours, underline the importance of geomagnetic control of *Es* layer occurrence.

Figure 7 depicts latitude-local time distributions of the occurrence rate of the COSMIC-retrieved *Es* layer for different seasons. In the northern and southern summer hemispheres, *Es* layers are prevalent at midlatitudes and predominantly occur during the period from 6 to around midnight local time (LT), with a salient reduction in the *Es* layer occurrence in the early morning hours between 3 and 6 LT. The patterns of the latitude-local time distributions of the *Es* layer in Northern and Southern Hemispheres for vernal season, which are basically symmetric with respect to the equator, are similar to those in the summer hemispheres. However, the minimum occurrence rates appear in the morning from about 6 to 10 LT, different from that of the summer hemisphere. For autumnal season, the *Es* layers occur primarily during evening from 15 to 22 LT. We will show later that the vertical propagations of the tidal waves with various periods are responsible for the patterns presented in Figure 7.

Figure 8 displays the monthly variation of the height-latitude distributions of the *Es* layer occurrence rates. It is clear that, for the southern summer (or northern winter) months from November to March, *Es* layers occur much higher and over a larger vertical extent in the Southern Hemisphere than those in Northern Hemisphere. For the northern summer (or southern winter) months from May to September, the patterns of the height-latitude

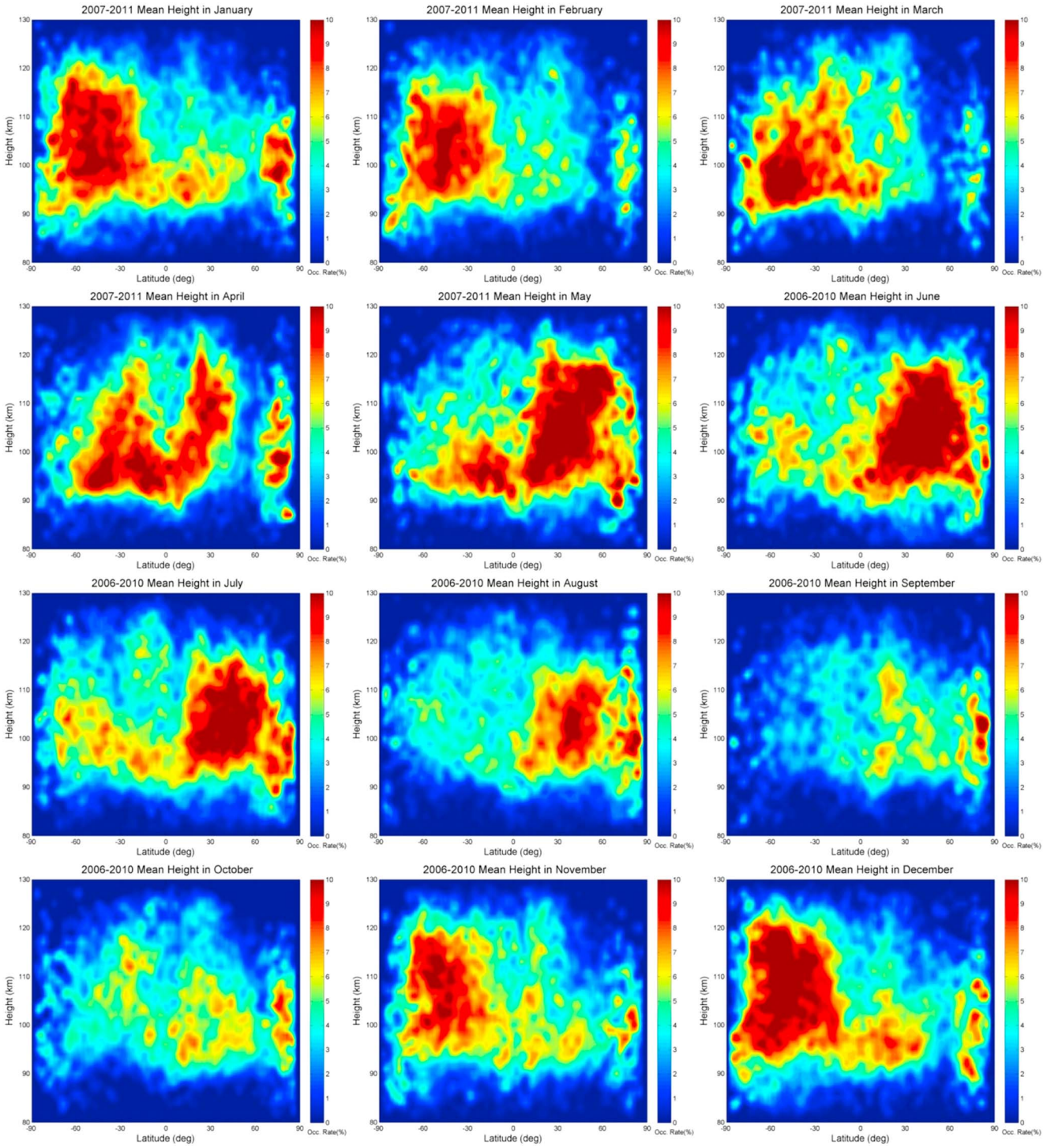

Figure 8. Seasonal variation in height-latitude distributions of occurrence rate of COSMIC-retrieved *Es* layer.

distributions of *Es* layer occurrence are opposite to those for the months from November to March. In general, the *Es* layer occurrence rate in the summer hemisphere is about 1.5–4 times greater than that in winter hemisphere, depending on month. Most *Es* layers occur primarily in the height range 95–120 km in the summer hemisphere and 95–100 km in the winter hemisphere, with a mean height 10–15 km higher for the former. For equinox months April and October, the height-latitude distributions of *Es* layer occurrences are generally symmetric with respect to the geomagnetic equator with similar height extent and occurrence rate.

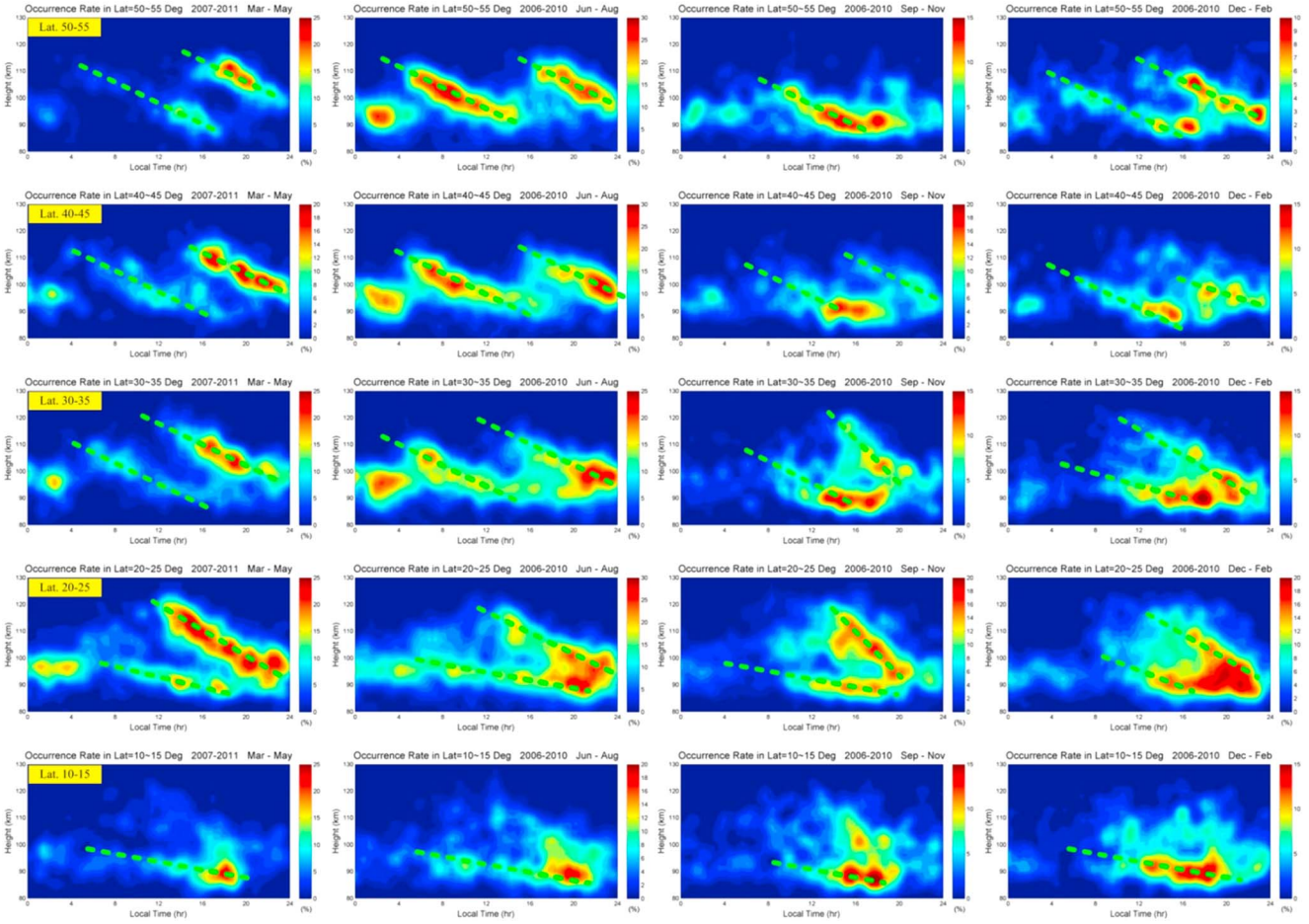

Figure 9. Seasonal variation in the height-local time distribution of the *Es* layer occurrence rates in different latitudinal regions for 2006–2008.

Figure 9 presents the seasonal variation in the height-local time distribution of the *Es* layer occurrence rates in different latitudinal regions in the Northern Hemisphere. The most striking feature is the semidiurnal behavior of the occurrence of *Es* layers that are prevalent at middle latitudes during spring and summer seasons in the Northern Hemisphere and descend with time from approximately 110 km down to 90 km at a rate of about 0.9–1.6 km/h. The starting times for the semidiurnal tide-associated *Es* layers to descend are approximately 6 and 18 LT, respectively. In general, the semidiurnal behaviors of the *Es* layer occurrence between Northern and Southern Hemispheres are very similar. A diurnal variation in *Es* layer occurrence can also be found in the height range 85–100 km at latitudes lower than 30° in spring and summer, where the semidiurnal behavior is not clearly discerned. The descending rate of the diurnal tide-associated *Es* layer is much smaller (about 0.6 km/h) than that of the semidiurnal tide-induced *Es* layer. In addition to the diurnal and semidiurnal tides, the terdiurnal tides that occur in a relatively narrow altitude range between about 90 and 100 km can also be seen in the midlatitude region ($>30°$).

Figure 10 shows the latitude-local time distributions of the *Es* layer occurrence rate at different heights for different seasons in 2007. The patterns of *Es* layer occurrence in different seasons for other years are in general similar to those of 2007. From Figure 10, in essence, there is no substantial hemisphere asymmetry in the patterns of the temporal occurrence of the *Es* layer in summer season, except for the magnitude of the occurrence rate. It is clear that the occurrences of *Es* layer in summer and spring seasons at midlatitudes ($>30°$) are controlled by the semidiurnal tides. The averaged extents of the *Es* layer occurrence patterns at midlatitudes in summer are about 45° in latitude and the patterns extend in their local time duration from 4 to more than 8 h during their descent from higher to lower altitudes. However, the *Es* layer occurrence patterns for northern and southern winter are governed by the diurnal tides with comparatively smaller

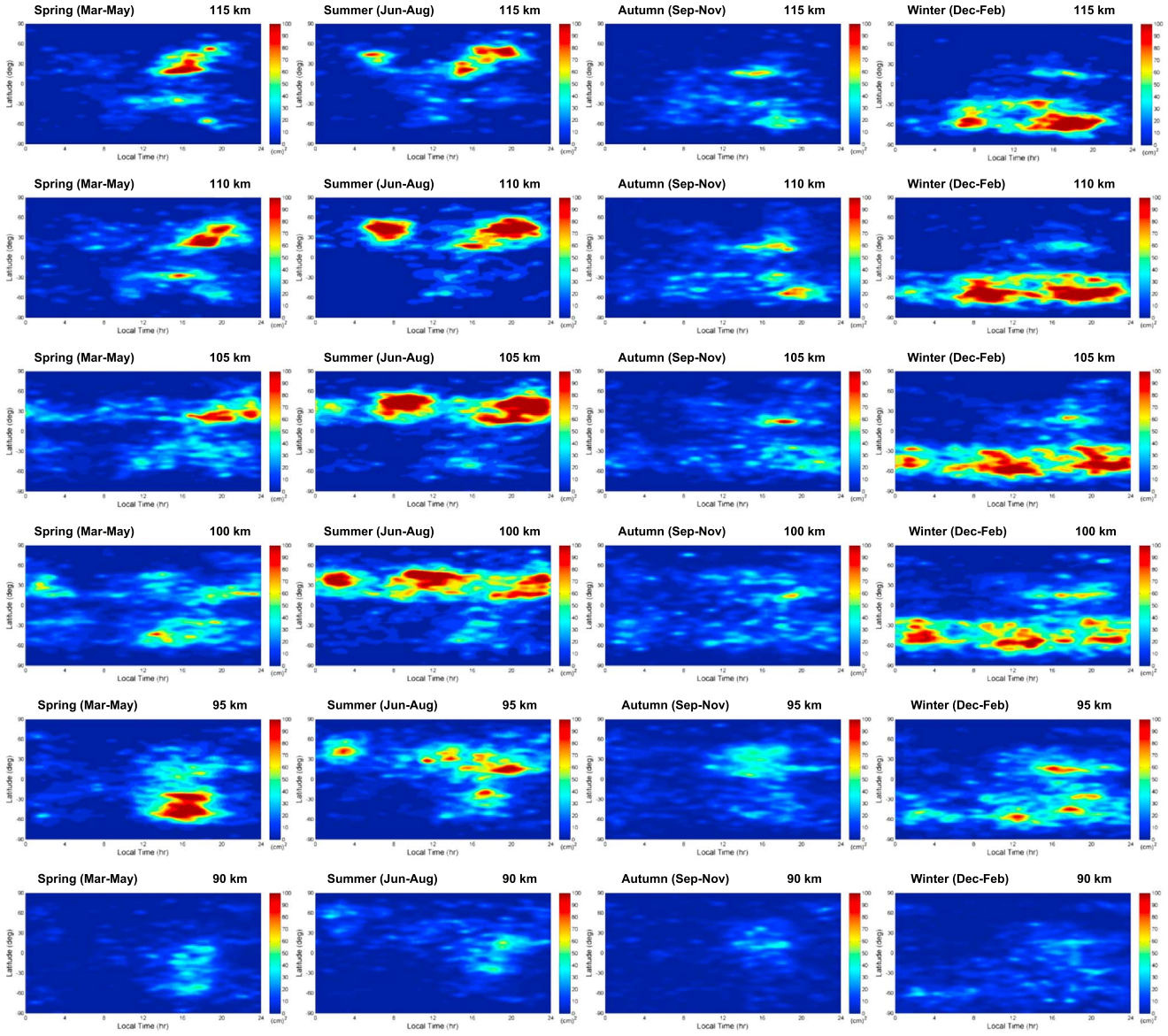

Figure 10. Latitude-local time distributions of the *Es* layer occurrence rate at different heights for different seasons in 2007, in which the second and fourth columns of the contour plots correspond to the *Es* layer occurrence in northern and southern summer seasons, respectively.

latitudinal span (20°–30°) and time duration (about 4–6 h) compared to summer. There is also a change in the pattern of *Es* layer occurrence toward the geomagnetic equator. At latitude below about 30° and altitudes lower than 100 km, the temporal occurrence of *Es* layers is dominated by the diurnal rather than the semidiurnal tide. It is noteworthy that during spring there is a remarked hemispheric asymmetry in the temporal *Es* layer occurrence: In Northern (Southern) Hemisphere, the occurrence is dominated by the semidiurnal (diurnal) tides, which is very different from those in the summer seasons. The temporal occurrences of the *Es* layers in autumnal season in both Northern and Southern Hemispheres are unclear because there is a paucity of COSMIC-measured *Es* layer data. From Figure 10, the terdiurnal tides can also be seen in the summer hemisphere in the height range 100–105 km, descending with time at a similar rate to the semidiurnal tide.

Figure 11 illustrates the longitudinal variation in the height-latitude distributions of the *Es* layer occurrence. The change of the distribution with longitude is not prominent, except for in the longitudinal sector near the Southern American Anomaly (SAA) region (i.e., approximately in the region between 30° S–60°S and 0°–60°E). Notice that the characteristics of *Es* layers in the SAA sector are very different from

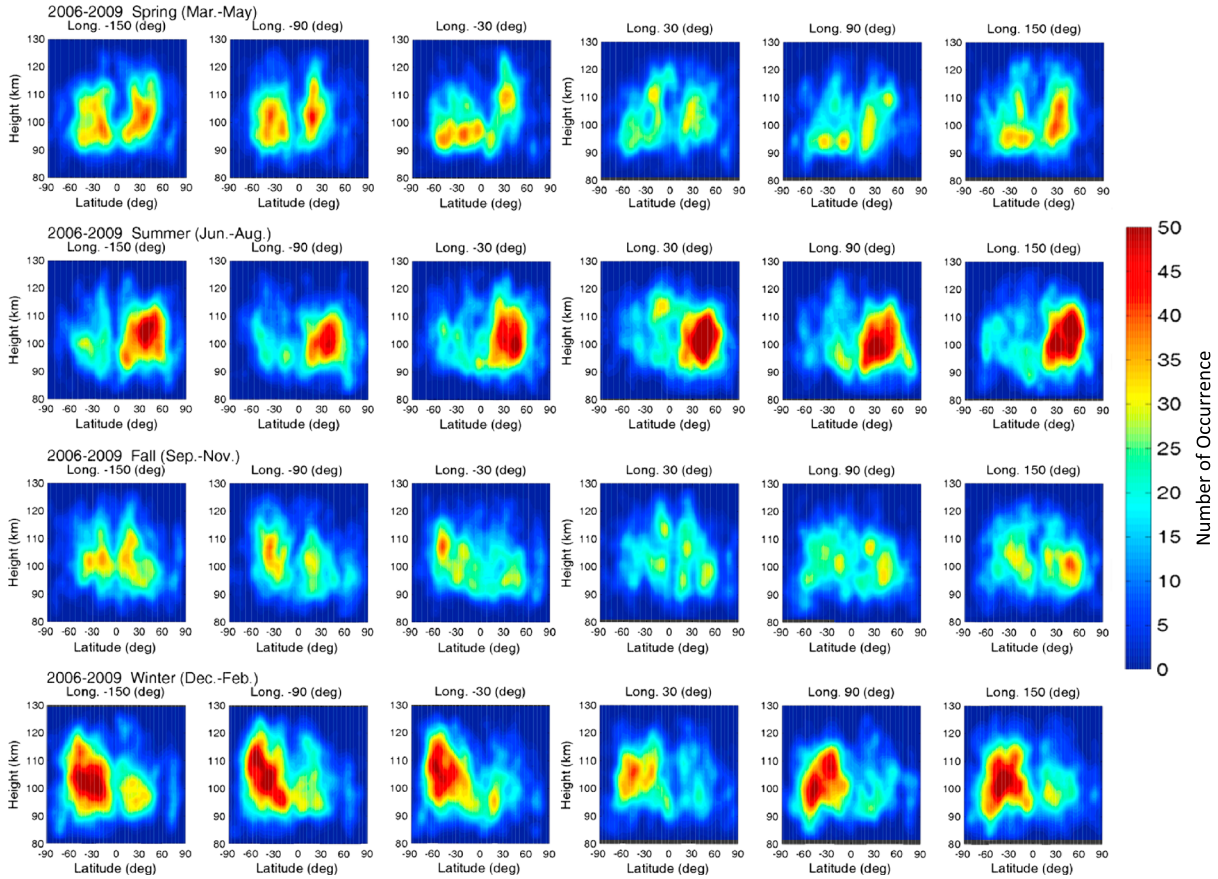

Figure 11. Longitudinal variation in height-latitude distributions of the *Es* layer occurrence.

other regions of the same longitude. The frequency of occurrence in this sector is significantly smaller. In addition, there is a tendency for the height range of the *Es* layer occurrence to be much wider in summer compared with winter. The hemispheric asymmetry in the height-latitude distribution patterns of the *Es* layer occurrences between the summer and winter seasons is also clearly seen in this longitudinal sector.

4. Wind Shear Theory Examination

Experimental observations and theoretical simulations both show that *Es* plasma irregularities can be generated by the various physical processes mentioned in section 1, which give rise to the amplitude and phase scintillations of the EM waves that travel through the plasma inhomogeneities with highly perturbed plasma densities or sharp vertical electron density gradients [*Om Vats et al.*, 1995; *Patel et al.*, 2009; *Zeng and Sokolovskiy*, 2010; *Patra et al.*, 2012]. In the context of GPS radio occultation measurement of the *Es* plasma irregularities, *Zeng and Sokolovskiy* [2010] showed that the scintillations in the amplitude and excess phase of the COSMIC-observed GPS RO signal result from the multipath interference effect of the direct and refracted GPS rays piercing through the horizontally extended thin *Es* layer with intense vertical electron density gradient on the top and bottom sides of the layer that is aligned with the path of the GPS ray. It is generally believed that the thin *Es* layer structure is very likely caused by the plasma convergence effect of the neutral wind shear through ion-neutral collision process [*Whitehead*, 1989; *Wang et al.*, 2011]. These results seem to imply that the neutral wind shear convergence effect is the cause of the *Es* layer structure detected by the COSMIC satellites employing the GPS RO technique. In the following, an examination is made to investigate the relation between COSMIC RO-detected *Es* layer and neutral wind shear.

From the wind shear theory, the vertical ion velocity w_i induced by the neutral wind is given by [*Nygren et al.*, 1984]

$$w_i = \frac{r\cos I}{1+r^2}V + \frac{\cos I \sin I}{1+r^2}U \quad (1)$$

where I is the magnetic inclination angle that is defined to be positive (pointing downward) in Northern Hemisphere, r is the ratio of ν_i (the ion-neutral collision frequency) to ω_i (the ion gyrofrequency), and V and U are, respectively, the components of the zonal (positive for eastward) and meridional (positive for northward) neutral wind. Note that the necessary condition for the wind profile that should be fulfilled to make the plasma converge in the wind shear zone is $I \neq 90°$ and $r\mathrm{d}V/\mathrm{d}z + \sin I \mathrm{d}U/\mathrm{d}z < 0$, which lead to $\mathrm{d}w_i/\mathrm{d}z < 0$. Therefore, the favorable wind profile for *Es* layer formation in the Northern Hemisphere will be where there is a negative in the zonal wind shear, i.e., a westward wind above and an eastward wind immediately below the *Es* layer. In the case of the meridional wind, a positive shear is required, i.e., a northward wind above and a southern wind below the *Es* layer.

As well as a favorable profile of the neutral wind shear, the existence of metallic ion with a sufficiently long lifetime even at high concentrations of electrons is another necessary condition for the formation of the *Es* layer at midlatitudes [*MacLeod et al.*, 1975; *Plane*, 2003]. Atomic ions such as Fe^+ and Mg^+ are the main constituents of the *Es* layer [*Kopp*, 1997; *Roddy et al.*, 2004; *Gregowsky and Aikin*, 2012]. They have lifetime in excess of 10^5 s above about 95 km, depending on the O_3, atomic O, and electron densities [*Woodcock et al.*, 2006; *Whalley et al.*, 2011], which is much longer than the timescale (from about several minutes to a few hours) required for the neutral wind to form the *Es* layer [*Brown*, 1973]. In addition, these metallic ion lifetimes are typically longer than the periods of the gravity waves and tides that can provide appropriate neutral wind profiles favoring the *Es* layer formation. Sounding rocket in situ measurement shows that the number densities of the metallic ions Fe^+ and Mg^+ are concentrated in the height range 85–115 km with peak concentrations of 10^3–10^5 cm^{-3} [*Kopp*, 1997]. Recently, *Feng et al.* [2013] have put the detailed chemistry of iron (eight neutral and four ionized iron-containing species with 30 neutral and ion-molecule reactions) into the Whole Atmosphere Community Climate Model (WACCM) to generate the global concentrations of nine iron-containing species including Fe^+. The meteoric input function, which describes the injection of Fe as a function of height, latitude, and day, is determined from an astronomical model coupled to a chemical meteoric ablation model [*Vondrak et al.*, 2008]. Figure 12 illustrates the global distributions of monthly mean concentration (top row) and zonal mean height profiles from 80 to130 km as a function of latitude (bottom row) of modeled Fe^+ for 2005–2011 simulated from WACCM-Fe [*Feng et al.*, 2013]. The WACCM-Fe model results, which are in reasonable accord with sparse rocket-borne measurements, show that the Fe^+ layer lies above 85 km with a maximum density of ~10^4 cm^{-3} close to 95 km. The latitudinal distribution of the Fe^+ column abundance exhibits hemispheric asymmetry with a maximum (minimum) at middle to high latitude in the summer (winter) hemisphere. Moreover, semiannual variations in the Fe^+ abundance can be seen at low latitudes, with a maximum at the equinoxes and minimum during the solstices.

On the basis of the WACCM-calculated Fe^+ concentrations combined with the Horizontal Wind Model (HWM07) and the Mass Spectrometer and Incoherent Scatter (MSIS-00) atmospheric model, the global distributions of the divergence of the vertical flux Φ_{Fe+} of the Fe^+ concentration are computed in accordance with the following expression

$$\nabla\Phi_{Fe^+} = n_{Fe^+}\frac{\mathrm{d}w_i}{\mathrm{d}z} + w_i\frac{\mathrm{d}n_{Fe^+}}{\mathrm{d}z} \quad (2)$$

where w_i is the vertical Fe^+ velocity driven by the neutral wind, which is estimated in accordance with 1. The monthly mean Fe^+ concentration and its vertical velocity are binned and averaged within a latitude-longitude-height grid that is 5° by 5° and by 1 km in size. Vertical difference of the product of the monthly mean values n_{Fe+} and w_i between adjacent grids is then calculated to obtain $\nabla\Phi_{Fe+}$ at the selected grids. Figure 13 presents model simulation results of the global distributions of the mean divergence of the Fe^+ concentration flux for height range 94–115 km for different seasons, in which negative (positive) value represents convergence (divergence) of the Fe^+ concentration flux in unit ions $m^{-2}\,s^{-1}\,km^{-1}$. Black and red curves in Figure 13 are magnetic latitudes and magnetic equator, respectively. A comparison between Figures 13 and 6 shows that the patterns of the model-simulated Fe^+ flux are well correlated to those of the COSMIC-measured *Es* layer occurrence. This result strongly suggests that the *Es* layers retrieved by the

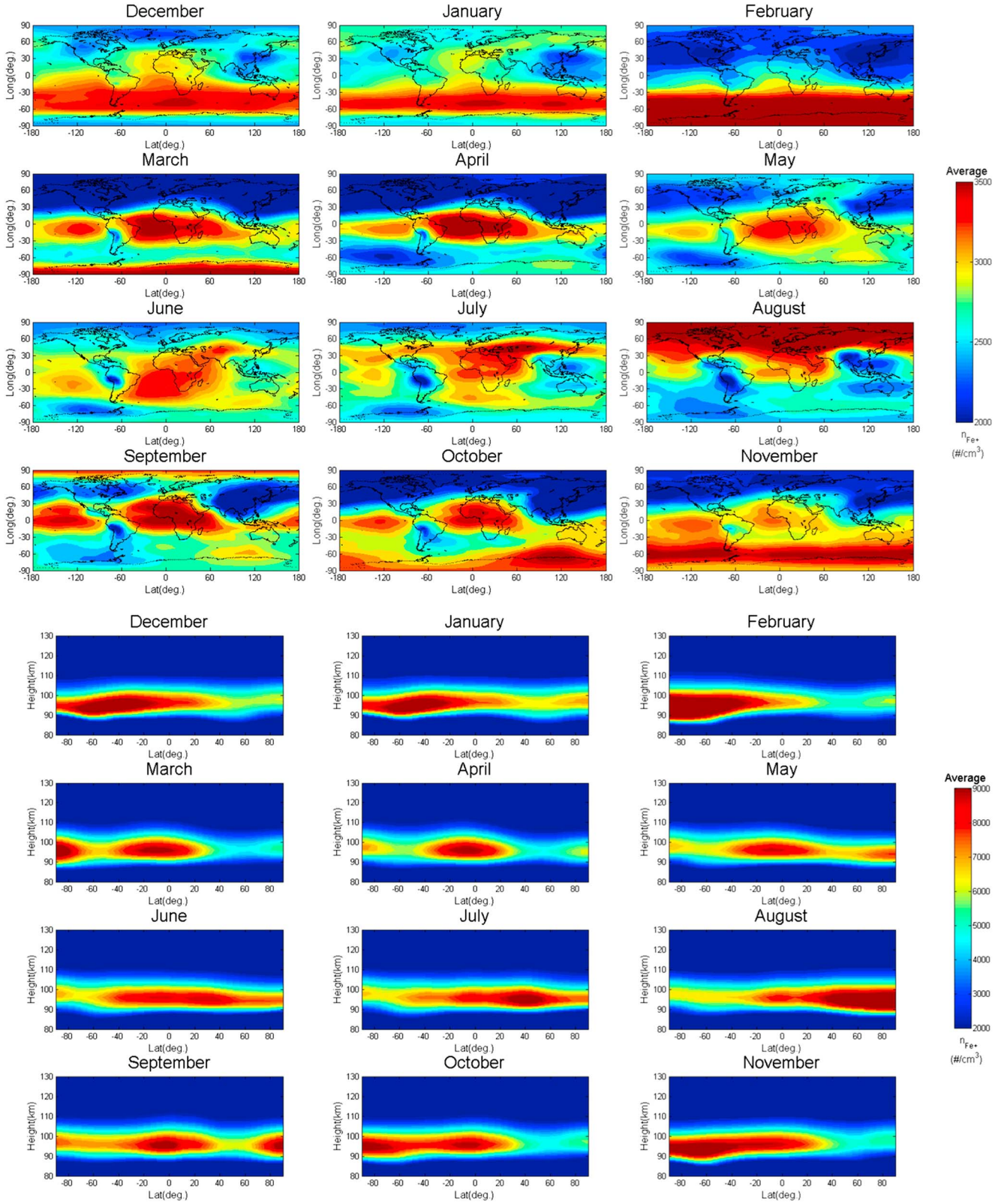

Figure 12. (top row) Monthly variations in the height-latitude distributions and (bottom row) height-latitude distributions of mean Fe^+ concentration in height range 80–130 km for 2005–2011.

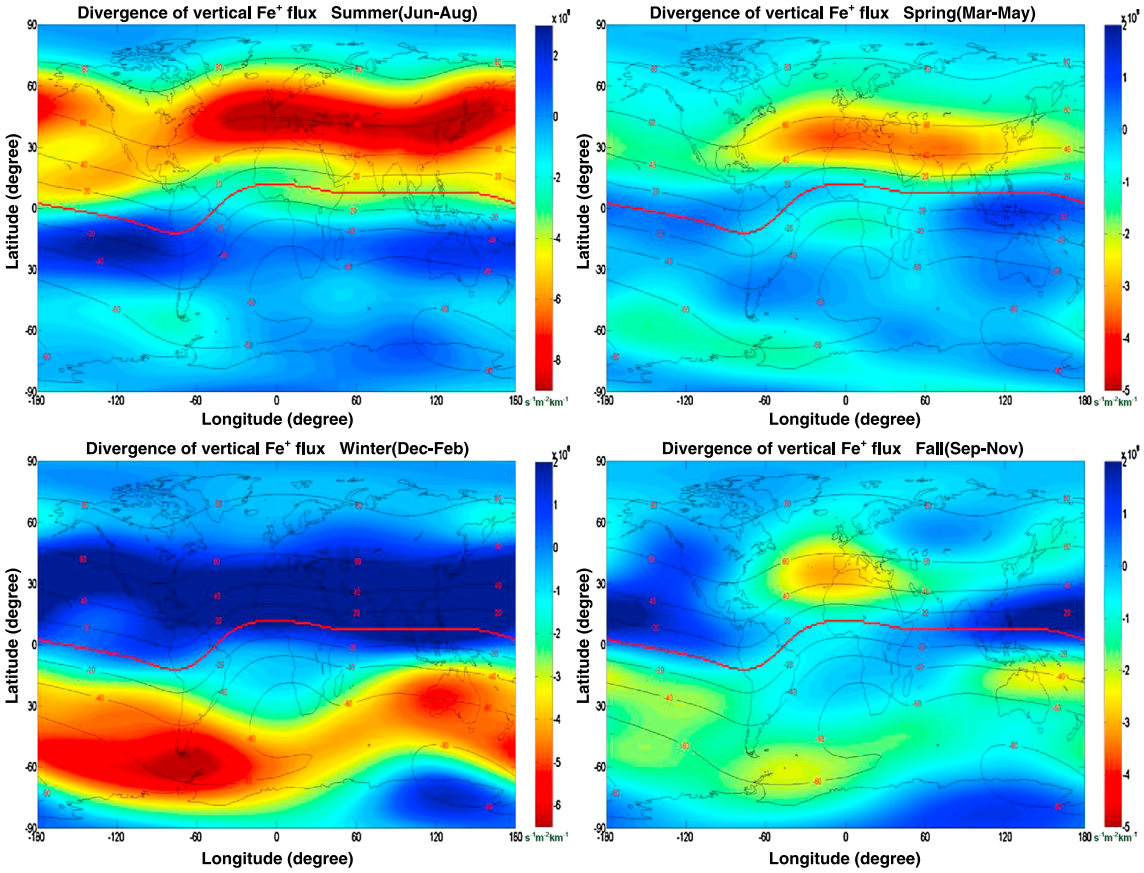

Figure 13. Simulation results of global distributions of divergence of vertical Fe^+ flux (in unit ions $m^{-2}\,s^{-1}\,km^{-1}$) in height range 95–114 km for different seasons. Black and red curves are magnetic latitudes and magnetic equator, respectively.

COSMIC satellites using GPS RO technique are primarily formed by the convergence effect of the neutral wind shear.

In addition to modeling the Fe^+ flux, we also compare the height-time distributions of *Es* layer occurrence with those of the neutral wind shear deduced from the HWM07 model. Figure 14 makes this comparison in three different latitude zones (53°–58°, 33°–38°, and 13°–18°) for different seasons. The white contour curves in Figure 14 represent the neutral wind shears, and the dashed lines signify the maximum wind shear zones that favor the formation of *Es* layers. The bottom row in Figure 14 depicts a comparison of the data collected in the southern summer (or northern winter) hemisphere. At midlatitudes, the *Es* layer occurrence regions are in complete accord with the neutral wind shear zones of the semidiurnal tides that dominate from 90 km to 120 km, especially in spring and summer. The occurrence of *Es* layers at low latitudes is also in general coincidence with the neutral wind shear zones below 100 km, where the diurnal tides dominate. However, the agreement is not good above 100 km at low latitudes, where the semidiurnal tides are much weaker compared to those in the midlatitude. Note that the neutral winds in the HWM07 model contain the wave number components 1–3 in solar local time, neutral wind components caused by short-period tides and gravity waves are not included in this model. It has long been known that gravity wave activity is much more active in equatorial and low-latitude regions (mainly within the latitude range ±20°) [*Tsuda et al.*, 2000; *Tsuda and Hocke*, 2004; *de la Torre et al.*, 2006; *Wang and Alexander*, 2010]. In addition, there is evidence that gravity wave may significantly affect the occurrence of RO-measured *Es* layer at low latitudes [*Hocke et al.*, 2001]. Thus, an explanation for the discrepancy between the *Es* layer occurrence and the neutral wind shear zone presented in Figure 14 is very likely the vertical propagations of the short gravity waves from below. However, more investigations on this subject are needed to validate this assertion.

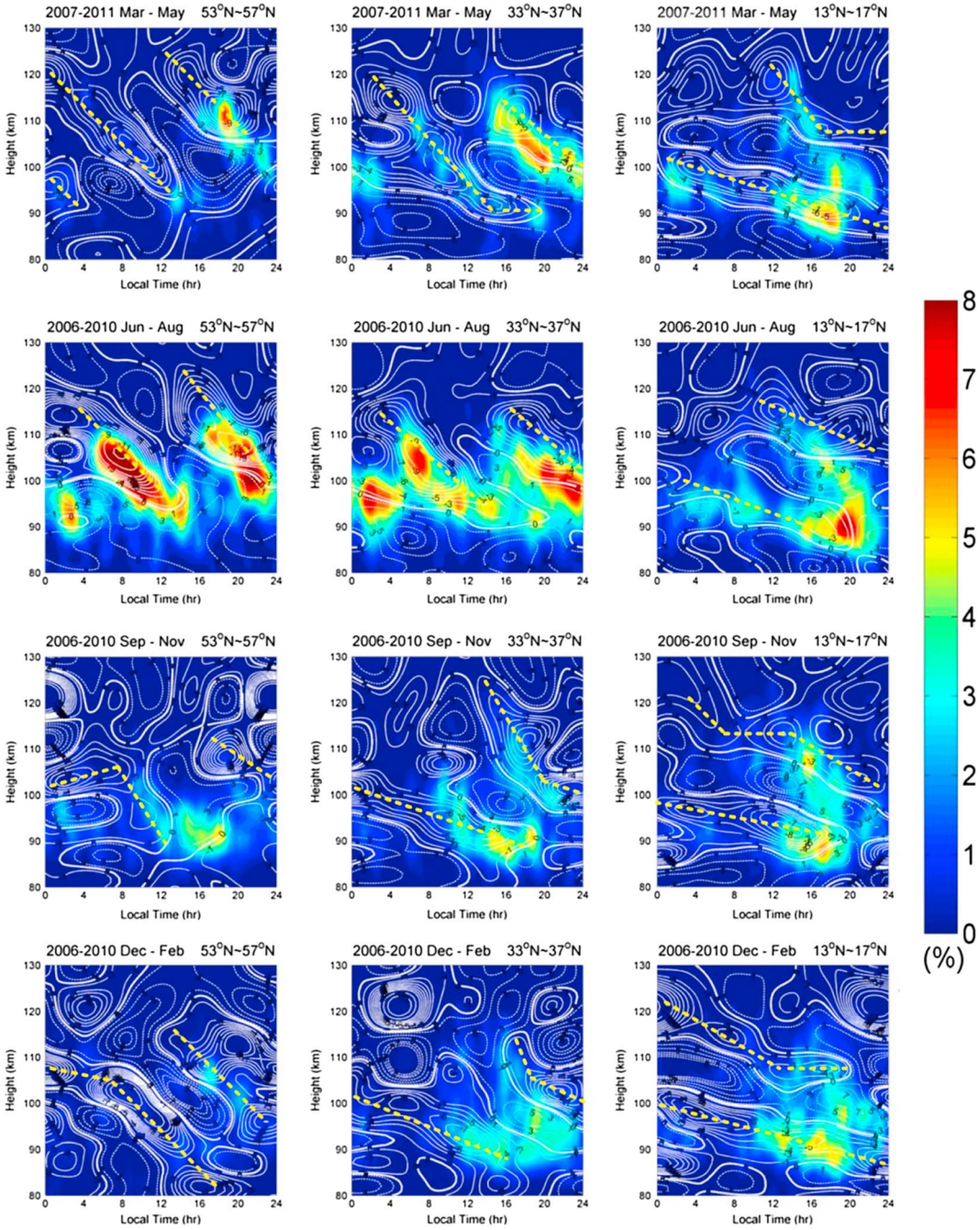

Figure 14. Comparison of height-latitude distribution of the *Es* layer occurrence with neutral wind shear derived from HWM07, in which solid (dotted) contours represent the wind shears that favor (hinder) the formation of *Es* layers.

5. Discussion

Figure 15 demonstrates the global distributions of the horizontal component intensity (left) and inclination angle (right) of the geomagnetic field at 100 km, estimated from International Geomagnetic Reference Field (IGRF) model. As shown in Figure 6, significant reductions in the *Es* layer occurrence around southern African and the Indian Ocean region in southern summer and the equinoxes are clearly present. *Arras et al*. [2008] attributed this reduction in *Es* layer occurrence to a severe decrease in the horizontal component of geomagnetic field. From 1, it is clear that, except for the geomagnetic horizontal component, the geomagnetic inclination angle *I* is also a crucial factor influencing the formation of *Es* layers via the wind shear mechanism. Figure 15

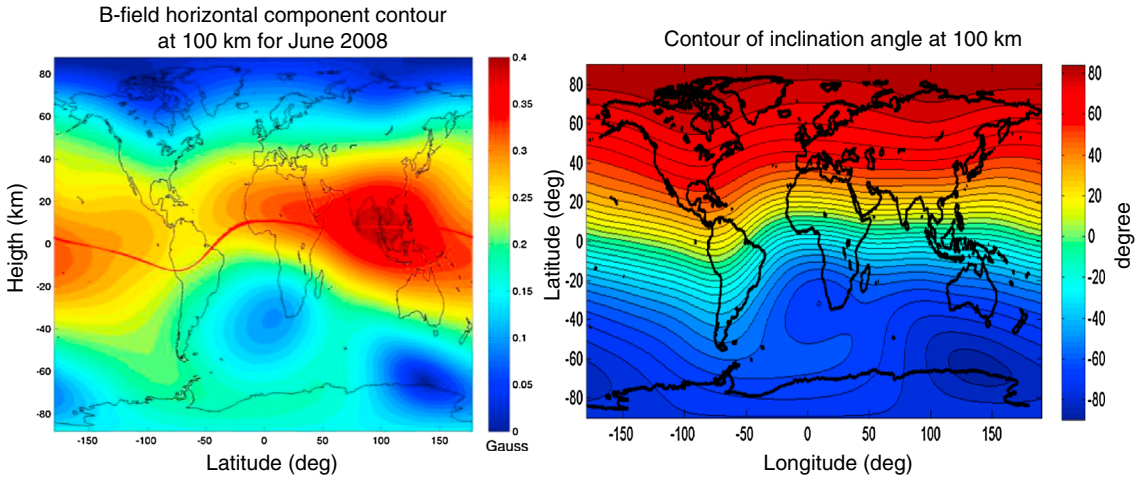

Figure 15. Global distributions of (left) horizontal component intensity and (right) inclination angle of geomagnetic field at 100 km estimated from IGRF model.

shows that, besides the SAA region, an appreciable decrease in the horizontal component and a very large inclination angle in the southern Australia area are seen. A comparison between Figures 6 and 15 indicates that there is no corresponding reduction in the *Es* layer occurrence rate in the southern Australia area. Instead, a substantial enhancement in the *Es* layer occurrence rate is found in this area during summer, which can also be seen in the data reported by *Arras et al.* [2008]. In addition, there is inconsistency between the *Es* layer occurrence rate and magnetic field factors in the eastern Asia and India sectors. This inconsistency between the magnetic field parameters and *Es* layer occurrence should be examined in future work.

In this study, we sift *Es* layer events from COSMIC-measured profiles of the GPS L1 and L2 SNRs and excess phases at a 1 Hz sampling rate. As shown in Figure 8, the *Es* layers occur majorly in the altitude range between 95 and 120 km in the summer hemisphere and between 95 and 100 km in the winter hemisphere. The former is about 10–15 km higher than the latter. *Arras et al.* [2008] utilized the GPS RO-measured SNR profiles at a 50 Hz sampling rate, most of which (about 90%) are collected by the COSMIC satellites and the rest are gathered by CHAMP and GRACE satellites, to select the *Es* layer events. Their results display that the summertime *Es* layers dominate at a height of 95–110 km and the wintertime *Es* layers mainly occur in the height range 90–105 km, with a peak occurrence height about 5 km higher for the former. Obviously, our results are higher than those obtained by *Arras et al.* [2008]. One of the reasons for the difference in the *Es* layer occurrence heights between the present study and *Arras et al.* [2008] is believed to be attributed to the limitation of the ceiling heights (mostly between 120 and 122 km) of the COSMIC profiles at a 50 Hz sampling rate. However, the top heights of the COSMIC-retrieved RO profiles at a 1 Hz sampling rate are well above the *E* region. Therefore, the *Es* layers that are extracted from the 1 Hz COSMIC RO profiles will not suffer from systematic bias in their height distribution.

As shown in Figure 6, *Es* layers occur abundantly at midlatitudes and are comparatively scarce in the geomagnetic equatorial belt of a few degrees width. These features can be explained in terms of the wind shear theory as shown in Figure 13. Note that the ionospheric plasma in the *Es* region (approximately between 90 and 120 km) is characterized by $\nu_i \sim \omega_i$ and $\nu_e \langle\langle \omega_e$ [*Rishbeth and Garriott*, 1969]. Assume that the neutral wind with constant vertical wind shear and the plasma density are both horizontally uniform. Because of differential collision rates between neutral-ion and neutral-electron particle pairs, there is a tendency for positive ions to leave the magnetic field lines where they originally reside, while the electrons (with the same number density as the ions) tend to remain along the original magnetic field lines. Therefore, for a westward (eastward) wind, the ions will move across the magnetic field line in the westward/downward (eastward/upward) direction and accumulate in the wind shear zone. When the ions are then captured by other magnetic field lines, the electrons that were separated from the ions at the original heights will be attracted by the positive ions and shift along the magnetic field lines to neutralize the positive ions. Consequently, the wind shear-induced *Es* layer can form in at midlatitudes, with charge neutrality maintained in the layer. Although this process for maintaining charge neutrality process is also applied to the plasma in a wind shear zone at the geomagnetic equator, there is no mechanism over the geomagnetic equator for the electrons at the upper

boundary of the wind shear zone, which become separated from the ions through differential neutral-ionization collision, to move across the nearly horizontal magnetic field lines to neutralize the positive ions that are generated at higher altitude and shift to the lower boundary of the wind shear zone. Subsequently, a vertically polarized electric field will be created in the wind shear zone which will hinder the vertical displacement of the positive ions, as shown in Figure 13 (bottom). Because of this, the wind shear-induced *Es* layer is very difficult to form at the geomagnetic equator [*Brown*, 1973; *Whitehead*, 1989].

On the basis of electron density fluctuations derived from the GPS RO-observed total electron content (TEC) in the *Es* region, *Hocke and Igarashi* [2002] presented the height-latitude distribution of the *Es* activity for summer and winter seasons. We note that the results obtained by *Hocke and Igarashi* [2002] are very different from those presented in Figure 8: Those workers did not report the infrequent occurrence of *Es* layers over the geomagnetic equator, nor the striking hemispheric asymmetry of *Es* layer occurrence at solstice. This suggests that the use of electron density fluctuations transformed from the RO-observed TEC does not capture *Es* layer events effectively.

It has long been suggested that lightning may affect the characteristics of *Es* layers, including an enhancement of the peak electron density and decrease in the layer height [*Johnson and Davis*, 2006]. However, a comparison of global distributions between COSMIC-retrieved *Es* layers, ground-based measurements of lightning events made by the World Wide Lightning Location Network and FORMOSAT-2-detected transient luminous events in the middle atmosphere seem to imply that the morphology of the COSMIC-retrieved *Es* layer bears no relation to lightning activities [*Lay et al*., 2007; *Chen et al*., 2008].

On the basis of the *Es* traces recorded by ionograms, the latitudinal distribution of the *Es* irregularities occurrence rate across the geomagnetic equator shows a maximum over the equator and a decrease with increasing geomagnetic latitude [*Rao*, 1964; *Oyinloye*, 1971; *Whitehead*, 1989; *Abdu et al*., 1996; *Tsunoda*, 2008]. This feature is obviously opposite to the phenomenon of minimum occurrence of GPS RO-retrieved *Es* layer over the equator, as shown in Figures 6 and 8. We have discussed above how the wind shear convergence mechanism dominates the formation of COSMIC-measured *Es* layers. This implies that most of the *Es* irregularities observed by ionosondes at the magnetic equator are likely generated by physical processes other than the wind shear mechanism, such as plasma instabilities and neutral turbulences.

6. Conclusion

In this study, we have investigated the morphology of the *Es* layers that are retrieved from the COSMIC-measured amplitude and excess phase scintillations of the GPS L1 and L2 signals at a 1 Hz sampling rate for data from June 2006 to May 2011. A data analysis scheme has been developed to select *Es* layers correctly from the measured data, in which the effects of *F* region irregularities, magnetic activity, background, and instrument noises on the GPS RO profiles are removed from the raw measurements.

Several *Es* layer properties presented in this paper, such as the summer maximum in *Es* layer occurrence at midlatitudes, infrequent occurrence of *Es* layers over the geomagnetic equator, depletion in *Es* layer occurrence in the area near the SAA region, and the diurnal variation of *Es* layer occurrence with a minimum in the morning and maximum in the afternoon and evening hours, are similar to those obtained in previous studies based on the GPS RO soundings with a 50 Hz sampling rate [*Wu et al*., 2005; *Arras et al*., 2008, 2010]. Nevertheless, a number of new results are presented in this paper. We find that *Es* layers that appear predominantly in middle- and low-latitude regions (10°–70°) are principally a summer phenomenon spanning from May to September in the Northern Hemisphere and from November to March in the Southern Hemisphere. The hemispheric asymmetry pattern of the *Es* layer height distribution—higher in summer hemisphere and lower in winter hemisphere—has the same period of 5 months as the latitudinal distribution. In addition, model simulations show that the physical process responsible for the summer maximum and winter minimum in the *Es* layer occurrence is very likely attributed to the convergence of metallic ion flux induced by the neutral wind shear in the *Es* region.

Acknowledgments
This work was supported by National Science Council (NSC) and National Space Program Organization (NSPO) of the Republic of China (Taiwan) under grants NSC 95-2111-M-008-015-MY3 and 98-NSPO(B)-IC-FA07-01(G), respectively. The WACCM-Fe model was supported by the UK Natural Environment Research Council (NERC grant NE/G019487/1). Robert Lysak thanks the reviewers for their assistance in evaluating this paper.

References

Abdu, M. A., I. S. Batista, P. Muralikrishna, and J. H. A. Sobral (1996), Long term trends in sporadic *E* layers and electric fields over Fortaleza, Brazil, *Geophys. Res. Lett.*, *23*, 757–760.

Arras, C., J. Wickert, G. Beyerle, S. Heise, T. Schmid, and C. Jacobi (2008), A global climatology of ionospheric irregularities derived from GPS radio occultation, *Geophys. Res. Lett.*, *35*, L14809, doi:10.1029/2008GL034158.

Arras, C., C. Jacobi, and J. Wickert (2009), Semidiurnal tidal signature in sporadic *E* occurrence rates derived from GPS radio occultation measurements at higher midlatitudes, *Ann. Geophys.*, *27*, 2555–2563.
Arras, C., C. Jacobi, J. Wickert, S. Heise and T. Schmidt (2010), Sporadic *E* signatures revealed from multi-satellite radio occultation measurements, *Adv. Radio Sci.*, *8*, 225–230.
Batista, I. S., and M. A. Abdu (1977), Magnetic storm associated delayed sporadic *E* enhancements in the Brazilian geomagnetic anomaly, *J. Geophys. Res.*, *82*, 4777–4783, doi:10.1029/JA082i029p04777.
Brown, T. L. (1973), The Chemistry of Metallic Elements in the Ionosphere and Mesosphere, *Chem. Rev.*, *73*, 645–667.
Chen, A. B., et al. (2008), Global distributions and occurrence rates of transient luminous events, *J. Geophys. Res.*, *113*, A08306, doi:10.1029/2008JA013101.
Chu, Y. H., and C. Y. Wang (1997), Interferometry observations of three-dimensional spatial structures of sporadic *E* irregularities using the Chung-Li VHF radar, *Radio Sci. 32*, 817–832.
Chu, Y. H., C. L. Su, and H. T. Ko (2010), A global survey of COSMIC ionospheric peak electron density and its height: A comparison with ground-based ionosonde measurements, *Adv. Space Res.*, *46*, 431–439.
Chu, Y. H., P. S. Brahmanandam, C.-Y. Wang, C.-L. Su and R.-M. Kuong (2011), Coordinated observations of sporadic *E* layer made with Chung-Li 30 MHz radar, ionosonde and FORMOSAT-3/COSMIC satellite, *J. Atmos. Sol. Terr. Phys.*, *73*, 883–894.
Clemesha, B. R. (1995), Sporadic neutral metal layers in the mesosphere and lower thermosphere, *J. Atmos. Terr. Phys.*, *57*, 72–736.
de la Torre, A., T. Schmidt, and J. Wickert (2006), A global analysis of wave potential energy in the lower stratosphere derived from 5 years of GPS radio occultation data with CHAMP, *Geophys. Res. Lett.*, *33*, L24809, doi:10.1029/2006GL027696.
Dou, X. K., X. H. Xue, T. Li, T. D. Chen, C. Chen, and S. C. Qiu (2010), Possible relations between meteors, enhanced electron density layers, and sporadic sodium layers, *J. Geophys. Res.*, *115*, A06311, doi:10.1029/2009JA014575.
Drob, D. P., et al. (2008), An empirical model of the Earth's horizontal wind fields: HWM07, *J. Geophys. Res.*, *113*, A12304, doi:10.1029/2008JA013668.
Farley, D. T. (1966), A theory of incoherent scattering of radio waves by a plasma 4. The effect of unequal ion and electron temperatures, *J. Geophys. Res.*, *71*(17), 4091–4098, doi:10.1029/JZ071i017p04091.
Farley, D. T. (1985), Theory of equatorial electrojet plasma waves: New developments and current status, *J. Atmos. Terr. Phys.*, *47*, 729–744.
Fejer, B. G., and M. C. Kelley (1980), Ionospheric irregularities, *Rev. Geophys. Space Phys.*, *18*, 401–454.
Fejer, B. G., J. Providakes, and D. T. Farley (1984), Theory of plasma waves in the auroral *E* region, *J. Geophys. Res.*, *89*, 7487–7494, doi:10.1029/JA089iA09p07487.
Feng, W., D. R. Marsh, M. P. Chipperfield, D. Janches, J. Hoffner, F. Yi and J. M. C. Plane (2013), A global atmospheric model of meteoric iron, *J. Geophys. Res. Atmos.*, *118*, 9456–9474, doi:10.1002/jgrd.50708.
Fritts, D. C., et al. (2010), Southern Argentina Agile Meteor Radar: System design and initial measurements of large-scale winds and tides, *J. Geophys. Res.*, *115*, D18112, doi:10.1029/2010JD013850.
From, W. R. and J. D. Whitehead (1986), *Es* structure using an HF radar, *Radio Sci.*, *21*, 309–312.
Grebowsky, J. M. and A. C. Aikin (2002), *In situ measurements of meteoric ions, in Meteors in the Earth's Atmosphere*, edited by E. Murat and I. P. Williams, pp. 189–214, Cambridge Univ. Press, Cambridge, U. K.
Gurevich, A. V., N. D. Borisov, and K. P. Zybin (1997), Ionospheric turbulence induced in the lower part of the *E* region by the turbulence of the neutral atmosphere, *J. Geophys. Res.*, *102*, 379–388, doi:10.1029/96JA00163.
Hajj, G. A., and L. J. Roman (1998), Ionospheric electron density profiles obtained with the Global Positioning System: Results from the GPS/MET experiment, *Radio Sci.*, *33*, 75–190.
Haldoupis, C., D. Pancheva, W. Singer, C. Meek, and J. MacDougall (2007), An explanation for the seasonal dependence of midlatitude sporadic *E* layers, *J. Geophys. Res.*, *112*, A06315, doi:10.1029/2007JA012322.
Hocke, K., and K. Igarashi (2002), Structure of the Earth's lower ionosphere observed by GPS/MET radio occultation, *J. Geophys. Res.*, *107*(A5), 1057, doi:10.1029/2001JA900158.
Hocke, K., and T. Tsuda (2001), Gravity waves and ionospheric irregularities over tropical convection zones observed by GPS/MET radio occultation, *Geophys. Res. Lett.*, *28*, 2815–2818.
Hocke, K., K. Igarashi, M. Nakamura, P. Wilkinson, J. Wu, A. Pavelyev, J. Wickert (2001), Global sounding of sporadic *E* layers by the GPS/MET radio occultation experiment, *J. Atmos. Sol. Terr. Phys.*, *63*, 1973–1980.
Janches, D., C. J. Heinselman, J. L. Chau, A. Chandran, R. Woodman (2006), Modeling the global micrometeor input function in the upper atmosphere observed by high power and large aperture radars, *J. Geophys. Res.*, *111*, A07317, doi:10.1029/2006JA011628.
Johnson, C. G., and C. J. Davis (2006), The location of lightning affecting the ionospheric sporadic *E* layer as evidence for multiple enhancement mechanisms, *Geophys. Res. Lett.*, *33*, L07811, doi:10.1029/2005GL025294.
Kelley, M. C. (1989), *The Earth's Ionosphere*, Academic Press, San Diego, Calif.
Kopp, E. (1997), On the abundance of metal ions in the lower ionosphere, *J. Geophys. Res.*, *102*, 9667–9674.
Larsen, M. F. (2000), A shear instability seeding mechanism for quasiperiodic radar echoes, *J. Geophys. Res.*, *105*, 24,931–24,940.
MacLeod, M. A., T. J. Keneshea, and R. S. Narcisi (1975), Numerical modelling of a metallic ion sporadic *Es* layer, *Radio Sci.*, *10*, 371–388.
Maruyama, T., S. Saito, M. Yamamoto, and S. Fukao (2006), Simultaneous observation of sporadic *E* with a rapid-run ionosonde and VHF coherent backscatter radar, *Ann. Geophys.*, *24*, 153–162.
Mathews, J. D. (1998), Sporadic *E*: Current views and recent progress, *J. Atmos. Sol. Terr. Phys.*, *60*, 413–435.
Mathews, J. D., D. Janches, D. D. Meisel, and Q.-H. Zhou (2001), The micrometeoroid mass flux into the upper atmosphere: Arecibo results and a comparison with prior estimates, *Geophys. Res. Lett.*, *28*, 1929– 1932.
Mukunda, M., and L. G. Smith (1968), Sporadic *E* classification from rocket measurements, *J. Atmos. Terr. Phys.*, *30*, 645–650.
Nygren, T., L. Jalonen, J. Oksman, and T. Turunen (1984), The role of electric field and neutral wind direction in the formation sporadic *E* layers, *J. Atmos. Terr. Phys.*, *46*, 373–381.
Om Vats, H., H. Chandra, M. R. Deshpande, and G. D. Vyas (1995), Radio star and satellite signal scintillation by *E* region irregularities: A case study, *Radio Sci.*, *30*, 475–478, doi:10.1029/94RS02924.
Patel, K., A. K. Singh, R. P. Patel, and R. P. Singh (2009), Characteristics of low latitude ionospheric *E*-region irregularities linked with daytime VHF scintillations measured from Varanasi, *J. Earth Syst. Sci.*, *118*, 721–732.
Patra, A. K., P. P. Chaitanya, and A. Bhattacharyya (2012), On the nature of radar backscatter and 250 MHz scintillation linked with an intense daytime E_s patch, *J. Geophys. Res.*, *117*, A03315, doi:10.1029/2011JA016981.
Plane, J. M. C. (2003), Atmospheric chemistry of meteoric metals, *Chem. Rev.*, *103*, 4963–4984.
Rao, C. S. R. (1964), Sporadic *E* and the equatorial electrojet, *J. Atmos. Terr. Phys.*, *29*, 417–427.
Rishbeth, H., and O. K. Garriott (1969), *Introduction to Ionospheric Physics*, 331 pp. Academic Press, San Diego, Calif.

Ritchie, S. E., and F. Honary (2009), Observations on the variability and screening effect of sporadic *E*, *J. Atmos. Sol. Terr. Phys.*, *71*, 1353–1364.
Roddy, P. A., G. D. Earle, C. M. Swenson, C. G. Carlson, and T. W. Bullett (2004), Relative concentrations of molecular and metallic ions in midlatitude intermediate and sporadic *E* layers, *Geophys. Res. Lett.*, *31*, L19807, doi:10.1029/2004GL020604.
Tsuda, T., and K. Hocke (2004), Application of GPS radio occultation data for studies of atmospheric waves in the middle atmosphere and ionosphere, *J. Meteorol. Soc. Jpn.*, *82*, 419–426.
Tsuda, T., M. Nishida, C. Rocken, and R. H. Ware (2000), A global morphology of gravity wave activity in the stratosphere revealed by the GPS occultation data (GPS/MET), *J. Geophys. Res.*, *105*, 7257–7273.
Tsunoda, R.T. (2008), On blanketing sporadic *E* and polarization effects near the equatorial electrojet, *J. Geophys. Res.*, *113*, A09304, doi:10.1029/2008JA013158.
Vondrak, T., J. M. C. Plane, S. L. Broadley, and D. Janches (2008), A chemical model of meteoric ablation, *Atmos. Chem. Phys.*, *8*, 7015–7031.
Wang, C. Y., Y. H. Chu, C. L. Su, R. M. Kuong, H. C. Chen, and K. F. Yang (2011), Statistical investigations of layer-type and clump-type plasma structures of 3-m field-aligned irregularities in nighttime sporadic *E* region made with Chung-Li VHF radar, *J. Geophys. Res.*, *116*, A12311, doi:10.1029/2011JA016696.
Wang, L., and M. J. Alexander (2010), Global estimates of gravity wave parameters from GPS radio occultation temperature data, *J. Geophys. Res.*, *115*, D21122, doi:10.1029/2010JD013860.
Whalley, C. L., J. C. G. Martin, T. G. Wright, and J. M. C. Plane (2011), A kinetic study of Mg^+ and Mg-containing ions reacting with O_3, O_2, N_2, CO_2, N_2O and H_2O: Implications for magnesium ion chemistry in the upper atmosphere, *Phys. Chem. Chem. Phys.*, *13*, 6352–6364.
Whitehead, J. (1961), The formation of the sporadic *E* layer in the temperate zone, *J. Atmos. Terr. Phys.*, *20*, 49–58.
Whitehead, J. (1989), Recent work on midlatitude and equatorial sporadic *E*, *J. Atmos. Terr. Phys.*, *51*, 401–424.
Woodcock, K. R. S., T. Vondrak, S. R. Meech, and J. M. C. Plane (2006), A kinetic study of the reactions $FeO^+ + O$, $Fe^+.N_2 + O$, $Fe^+.O_2 + O$ and $FeO^+ + CO$: Implications for sporadic *E* layers in the upper atmosphere, *Phys. Chem. Chem. Phys.*, *8*, 1812–1821.
Wu, D. L. (2006), Small-scale fluctuations and scintillations in high-resolution GPS/CHAMP SNR and phase data, *J. Atmos. Sol. Terr. Phys.*, *68*, 999–1017.
Wu, D. L., C. O. Ao, G. A. Hajj, M. T. Juarez, and A. J. Mannucci (2005), Sporadic *E* morphology from GPS-CHAMP radio occultation, *J. Geophys. Res.*, *110*, A01306, doi:10.1029/2004JA010701.
Yang, K. F., Y. H. Chu, C. L. Su, H. T. Ko, and C. Y. Wang (2009), An examination of FORMOSAT-3/COSMIC *F* peak and topside electron density measurements: Data quality criteria and comparisons with the IRI model, *Terr. Atmos. Oceanic. Sci.*, *20*, 193–206.
Yinn-Nien, H. (1965), Geomagnetic activity and occurrence of sporadic *E* in the Far East, *J. Geophys. Res.*, *70*, 1187–1194, doi:10.1029/JZ070i005p01187.
Zeng, Z., and S. Sokolovskiy (2010), Effect of sporadic *E* clouds on GPS radio occultation signals, *Geophys. Res. Lett.*, *37*, L18817, doi:10.1029/2010GL044561.